Monthly Notices of the ROYAL ASTRONOMICAL SOCIETY

MNRAS **469,** 3518–3531 (2017) doi:10.1093/mnras/stx1102
Advance Access publication 2017 May 6

# ALMA observations of the multiplanet system 61 Vir: what lies outside super-Earth systems?

S. Marino,[1]★ M. C. Wyatt,[1] G. M. Kennedy,[1] W. Holland,[2] L. Matrà,[1] A. Shannon[3,4] and R. J. Ivison[5,6]

[1]*Institute of Astronomy, University of Cambridge, Madingley Road, Cambridge CB3 0HA, UK*
[2]*UK Astronomy Technology Centre, Royal Observatory, Blackford Hill, Edinburgh EH9 3HJ, UK*
[3]*Department of Astronomy and Astrophysics, The Pennsylvania State University, State College, PA 16801, USA*
[4]*Center for Exoplanets and Habitable Worlds, The Pennsylvania State University, State College, PA 16802, USA*
[5]*Institute for Astronomy, University of Edinburgh, Royal Observatory, Edinburgh EH9 3HJ, UK*
[6]*European Southern Observatory, Karl-Schwarzchild-Str. 2, D-95748 Garching b. Munchen, Germany*

Accepted 2017 May 4. Received 2017 May 4; in original form 2017 March 3

## ABSTRACT

A decade of surveys has hinted at a possible higher occurrence rate of debris discs in systems hosting low-mass planets. This could be due to common favourable forming conditions for rocky planets close in and planetesimals at large radii. In this paper, we present the first resolved millimetre study of the debris disc in the 4.6 Gyr old multiplanet system 61 Vir, combining Atacama Large Millimeter/submillimeter Array and James Clerk Maxwell Telescope data at 0.86 mm. We fit the data using a parametric disc model, finding that the disc of planetesimals extends from 30 au to at least 150 au, with a surface density distribution of millimetre-sized grains with a power-law slope of $0.1^{+1.1}_{-0.8}$. We also present a numerical collisional model that can predict the evolution of the surface density of millimetre grains for a given primordial disc, finding that it does not necessarily have the same radial profile as the total mass surface density (as previous studies suggested for the optical depth), with the former being flatter. Finally, we find that if the planetesimal disc was stirred at 150 au by an additional unseen planet, that planet should be more massive than 10 $M_\oplus$ and lie between 10 and 20 au. Lower planet masses and semimajor axes down to 4 au are possible for eccentricities $\gg$0.1.

**Key words:** circumstellar matter – stars: individual: HD 115617 – planetary systems – radio continuum: planetary systems.

## 1 INTRODUCTION

Planetary systems around main-sequence stars are not only composed of planets; planetesimal belts can be also present, analogous to the Kuiper belt (at tens of astronomical units) and the Asteroid belt (within a few astronomical units) in the Solar system. These belts can produce dusty debris discs as the result of a so-called collisional cascade (e.g. Dominik & Decin 2003; Wyatt et al. 2007), where solids in a wide size distribution from μm-sized grains up to km-sized planetesimals are ground down in collisions, sustaining high levels of dust and infrared excess over Gyr time-scales. Debris discs at tens of astronomical units are fairly common around FGK stars, with occurrence rates of at least ∼20 per cent (e.g. Su et al. 2006; Hillenbrand et al. 2008; Carpenter et al. 2009; Eiroa et al. 2013; Matthews et al. 2014a; Thureau et al. 2014; Montesinos et al. 2016); therefore, a complete understanding of their properties can give us information about planet formation and migration history of planets in these systems (e.g. Wyatt 2006).

Moreover, a few systems are known to host both a planet(s) and a debris disc(s). Among the best studied are $\beta$ Pic (e.g. Smith & Terrile 1984; Lagrange et al. 2009; Dent et al. 2014), HR 8799 (e.g. Marois et al. 2008, 2010; Matthews et al. 2014b; Booth et al. 2016) and Fomalhaut (e.g. Kalas et al. 2008), all with planets directly imaged and lying between the star and the disc. However, these systems are outliers in terms of their planets and disc properties and neither represents the bulk of the known planetary systems, nor debris discs.

Thanks to unbiased debris disc surveys of FGK stars within 45 pc (e.g. DUNES and DEBRIS; Eiroa et al. 2013; Matthews et al. 2014a), it has been possible to study the frequency of circumstellar material around stars hosting high- and low-mass planets detected by radial velocity (RV) surveys. Studies focused on high-mass planets found no evidence of a different debris disc incidence rate in these planet hosting stars compared to normal field stars (Greaves et al. 2004; Moro-Martín et al. 2007; Bryden et al. 2009). On the

★E-mail: sebastian.marino.estay@gmail.com

other hand, two studies focused on planetary systems with planet masses below ∼95 $M_\oplus$ found debris disc incidence rates of: 4/6 (Wyatt et al. 2012), significantly higher compared to field stars; and 2/6 (Moro-Martín et al. 2015), consistent with field stars. Combining both samples, at least four out of eight systems with low-mass planets also have a debris disc, which suggests that there might be a difference in the occurrence of bright debris discs in systems with low-mass planets, as predicted by planet formation models (e.g. Raymond et al. 2011).

One of these planetary systems hosting a debris disc is 61 Vir. This system located at 8.6 pc (van Leeuwen 2007) is composed of : (1) a G5 4.6 ± 0.9 Gyr old star (Wright et al. 2011; Vican 2012); (2) three RV planets of minimum masses 5, 18 and 23 $M_\oplus$ and semimajor axes of 0.05, 0.22 and 0.49 au, respectively (Vogt et al. 2010, the third one was not confirmed in the HARPS data; Wyatt et al. 2012); and (3) a debris disc discovered by *Spitzer* with a fractional luminosity $L_{\rm disc}/L_\star$ of $2 \times 10^{-5}$ (Bryden et al. 2006). The disc was later imaged by *Herschel* showing that the disc density peaks between 30 and 100 au and it is inclined by ∼77° with respect to the plane of the sky (Wyatt et al. 2012). If disc and orbits of these planets are co-planar, then the planet masses would be only underestimated by 3 per cent. This system is particularly interesting as the fraction of stars with super-Earths, similar to 61 Vir, could be up to 30–50 per cent (e.g. Howard et al. 2010; Mayor et al. 2011; Fressin et al. 2013), which makes 61 Vir a good case to study the formation of such abundant planets by analysing its debris disc.

Due to a low 50 au resolution, *Herschel* could not constrain the exact morphology and dust distribution at the inner regions of the disc, but by image and spectral energy distribution (SED) fitting Wyatt et al. (2012) found three best-fitting models: (1) an extended disc with a sharp inner edge at ∼30 au, extending at least out to 100 au, and a surface density or optical depth radial profile with an exponent of −1.1; (2) similar to the first model, but adding an inner component where the surface density increases with radius as $r^{7/3}$ (inspired by collisional evolution models) from 1 au to the disc inner edge now placed at 43 au; (3) a two belt model consisting of two 10 au wide dusty belts centred at 40 and 90 au. These three models could well fit the previous observations, but the low 50 au resolution hindered determining the exact dust distribution. Moreover, because the disc emission at *Herschel* wavelengths is dominated by small grains that are subject to radiation forces, the derived distribution does not necessarily trace the location of the parent planetesimal belt, as they can extend to larger radii beyond that belt (e.g. Thébault & Augereau 2007).

In this paper, we present the first observations of 61 Vir with the Atacama Large Millimeter/submillimeter Array (ALMA) at 0.86 mm, obtained with the aim of studying its debris disc to reveal the location of the parent planetesimals, and place constraints on the presence of planets at large separations that can shape the mass distribution in the disc. Because radiation forces are negligible for mm-sized grains, their distribution can be used to trace the location of the biggest km-sized planetesimals (or bigger), which contain the bulk of the disc mass and sustain the collisional cascade. At millimetre wavelengths, the dust thermal emission is dominated by mm-sized grains (∼0.1–10 mm); therefore, observations with ALMA are well suited to study the dynamics and origin of debris discs. In order to obtain the best disc constraints, in our analysis we combine new ALMA band seven observations and new data at 0.85 mm from the Sub-millimetre Common-User Bolometer Array 2 (SCUBA2) installed in the James Clerk Maxwell Telescope (JCMT), thus, incorporating information from small and large angular scale structure.

In addition, we implement a simple numerical collisional evolution model that simulates the evolution of a broad disc, taking into account the disruption threshold of planetesimals as a function of size, how relative velocities vary with radii and the different features in the size distribution of solids, e.g. the ripples close to the blow-out size. We use this to constrain the initial solid mass or surface density in the disc and the maximum planetesimal size.

This paper is organized as follows. In Section 2, we present new SCUBA2/JCMT data. In Section 3, we describe the ALMA observations, studying the dust continuum and how it compares with previous *Herschel* observations. We also search for CO ($v = 0$, J = 3–2) line emission. In Section 4, we fit the SCUBA and ALMA data using a parametric disc model to study the distribution of millimetre dust in the disc. Section 5 describes a numerical model to calculate the collisional evolution of a disc at different radii that can be used to compare with observations determining the maximum planetesimal size in a disc and the initial solid mass. In Section 6, we discuss the observations and possible scenarios that could explain the low initial solid mass and maximum planetesimal size. Moreover, we constrain the mass, semimajor axis and eccentricity of a hypothetical planet stirring the disc. Finally, in Section 7 we summarize and present the main conclusions of this paper.

## 2 SCUBA2 OBSERVATIONS

As part of the SCUBA-2 Observations of Nearby Stars (SONS) survey (Panić et al. 2013), 61 Vir was observed at 0.85 mm with SCUBA2/JCMT (Holland et al. 2013) to constrain the millimetre flux and extent of its debris disc. 61 Vir was observed for 7.5 h and the data were reduced using the Dynamic Iterative Map-Maker within the Starlink SMURF package (Chapin et al. 2013), which was called from the automated pipeline ORAC-DR (Cavanagh et al. 2008). More details on the SCUBA2 data reduction of the SONS survey can be found in Matthews et al. (2015) and Kennedy et al. (2015).

*Herschel* and Very Large Array (VLA) observations previously found three background sources close to 61 Vir that could affect our analysis of the SCUBA2 data. To obtain a non-contaminated large-scale image and photometry of 61 Vir, we subtract these as point sources, using as point spread function (PSF) the SCUBA2 reduced observation of Uranus obtained in the same run. As two of these sources are detected in the ALMA data (see Section 3.1), we can derive their fluxes and astrometric positions at 0.86 mm, and accurately subtract these from the SCUBA2 reduced image, correcting for the proper motion of 61 Vir $\mu = (1.07, -1.06)$ arcsec yr$^{-1}$ (van Leeuwen 2007). The third background and more distant source from 61 Vir is not detected with SCUBA2, and lies outside the field of view of the ALMA observations. In Fig. 1, we present the SCUBA2 image smoothed with a Gaussian kernel of full width at half-maximum (FWHM) 6.5 arcsec after subtracting the two background sources. Integrating all the emission inside a circumference of 15 arcsec radius, we find a total flux of 5.0 ± 1.2 mJy (including the stellar emission and calibration uncertainty), slightly lower but consistent within errors with the previous data presented in Panić et al. (2013).

## 3 ALMA OBSERVATIONS

ALMA band 7 (0.86 mm) observations of 61 Vir were carried out on 2015 April, split into four scheduling blocks (one on April 9 and three on April 22) as part of the project 2013.1.00359.S (PI: M.C. Wyatt). The total number of antennas was 44, with baselines ranging

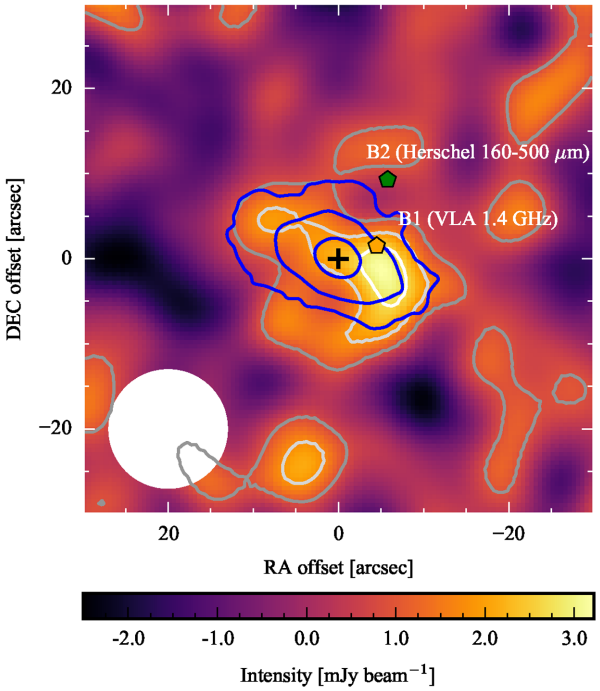


**Figure 1.** SCUBA2 0.85 mm continuum image of 61 Vir after subtracting two point sources from background emission. The beam size is 13 arcsec and is represented with a white ellipse at the bottom left corner of the image. The grey and white contours represent emission above one, two and three times the noise level. Blue contours at arbitrary levels from the *Herschel* 70 μm image are overlaid and are corrected for proper motion. The green and yellow pentagon symbols indicate the position of the background sources that were subtracted from this image. The *x*- and *y*-axes indicate the offset from the stellar position in RA and Dec. in arcsec, i.e. north is up and east is left. The stellar position is marked with a black '+'.

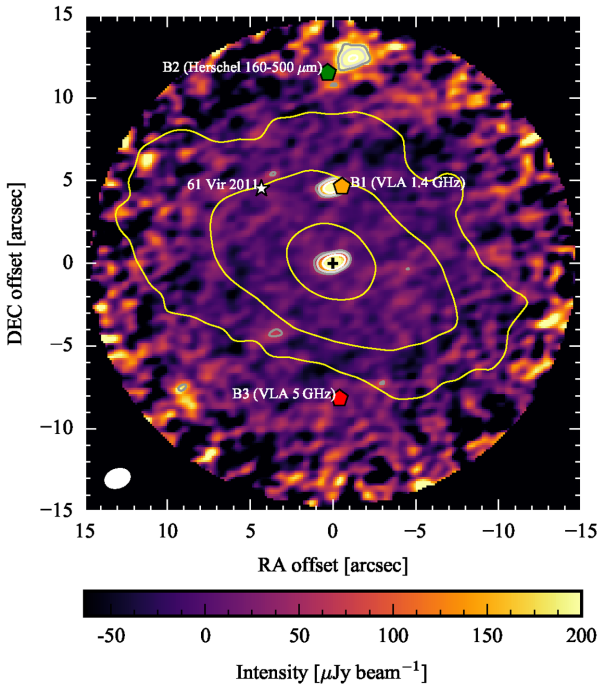


**Figure 2.** ALMA band 7 (0.86 mm) continuum image of 61 Vir with natural weights and corrected by the primary beam response (FWHM ∼ 17 arcsec). The beam size is 1.1 arcsec × 0.7 arcsec and is represented with a white ellipse at the bottom left corner of the image. The grey and white contours represent emission above 3, 5 and 10 times the local noise level. Yellow contours from the *Herschel* 70 μm image at arbitrary levels are overlaid correcting by the stellar proper motion. The *x*- and *y*-axes indicate the offset from the stellar position in RA and Dec. in arcsec, i.e. north is up and east is left. The stellar position is marked with a black '+' and the position of background sources previously detected are represented with pentagons. The black masked region indicates a primary beam response below 10 per cent.

from 15 to 349 m, with 5th and 95th percentiles equivalent to 29 and 228 m. This allows us to recover angular scales of 0.6 arcsec up to 6 arcsec on the sky.

The correlator was set up with three spectral windows to image the continuum centred at 333.84, 335.78 and 347.74 GHz, each with 128 channels and a total bandwidth of 1.88 GHz; and a fourth one to search for CO ($v = 0$, J = 3–2) emission in the disc centred at 344.85 GHz, with 3840 channels, a channel width of 0.42 km s$^{-1}$ (effective spectral resolution of 0.82 km s$^{-1}$) and a total bandwidth of 2 GHz.

In all of the scheduling blocks, J1337−1257 was used as bandpass and phase calibrator, with Titan as amplitude and flux calibrator. Calibrations were applied using the pipeline provided by ALMA. The total time on source excluding overheads was 178 min.

### 3.1 Continuum emission

To study the continuum emission, we use the four spectral windows to reach the highest sensitivity as no CO emission is present in the data (this is discussed below). Fig. 2 shows the continuum image using the task CLEAN in CASA 4.4 (McMullin et al. 2007) with natural weights and correcting for the primary beam – note that the noise increases towards the edges of the image as the primary beam sensitivity decreases. At the centre of the image, we achieve an rms noise level of 16 μJy beam$^{-1}$, which increases to 32 μJy beam$^{-1}$ at 7.5 arcsec. The beam size is 1.1 arcsec × 0.7 arcsec with a position angle (PA) of −70°. In the image, three compact sources are detected: 61 Vir's stellar emission at the centre with a total flux of 374 ± 16 μJy, which is 2.4$\sigma$ higher than the 320 ± 16 μJy predicted photospheric emission assuming a spectral index of −2, thus, it could be due to chromospheric emission at this wavelength (e.g. Loukitcheva et al. 2004; Fontenla, Balasubramaniam & Harder 2007); and two other sources to the north of the star with offsets of 4.5 and 12.5 arcsec, and peak fluxes of 360 ± 20 and 850 ± 70 μJy, respectively. The latter is resolved with a total flux of 2.2 ± 0.3 mJy within a 2 arcsec radius circumference. These two sources are almost certainly the background galaxies previously reported in Wyatt et al. (2012) and their position is overlaid with pentagon markers and labelled as B1 and B2. We also overlay the position of a third background source (B3) detected at 5 GHz with the VLA and not present in the ALMA data. The latter is the southern component of a double-lobed structure with the northern component outside the ALMA primary beam. At 1.4 GHz, B1 was marginally resolved and found to be extended in the north–south direction with a fitted FWHM of 33 arcsec, therefore, consistent as being the two lobes resolved at 5 GHz.

Although there is no disc emission above 3$\sigma$ in the ALMA CLEAN image, significant signal is present in the real component of the visibilities after subtracting the three compact sources. By de-projecting the observed visibilities assuming a disc PA and inclination of 65° and 77°, respectively (consistent with the *Herschel* observations; Wyatt et al. 2012), we recover disc emission in the short baselines ($\lesssim$10 kλ, see Fig. 3) corresponding to extended emission

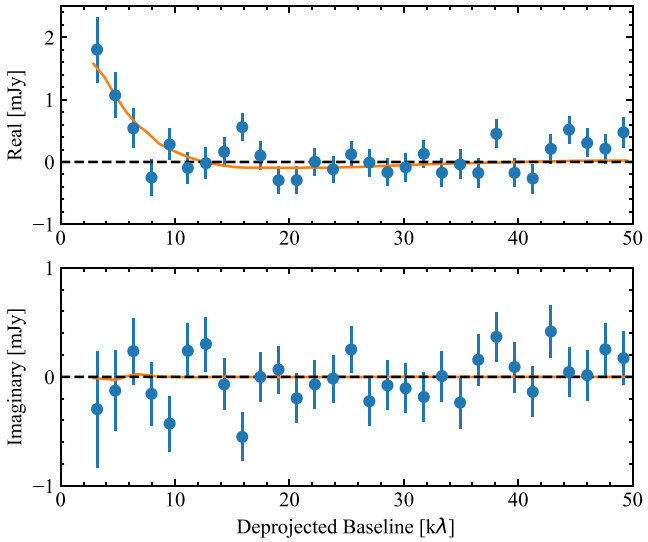


**Figure 3.** Deprojected visibility profile of the ALMA band 7 (0.86 mm) continuum after subtracting the emission from the three compact sources. The blue points represent averaged and binned visibilities with $1\sigma$ error bars. Overlaid is a best-fitting disc model (orange line).

($\gtrsim$20 arcsec or 150 au). We also overlay the model visibilities of a disc with a flux of 4 mJy and extending from 30 to 140 au, consistent with the data (see Section 4). The imaginary part of the visibilities is consistent with pure noise around zero, which is expected for an axisymmetric centred disc.

We can also recover the disc emission in the image space by integrating the flux inside ellipses of different semimajor axes (with the same PA and aspect ratio or inclination as the disc resolved by *Herschel*). In this integration, we also exclude a 30° wide wedge in the direction of B1. The resulting radial profile is presented in the top panel of Fig. 4. Within 10 arcsec, the total disc and stellar emission is only $0.8 \pm 0.2$ mJy, $2.2\sigma$ lower than the derived flux from SCUBA2. If we subtract the stellar emission, the disc is marginally detected at $2.2\sigma$ with a total flux of $0.43 \pm 0.2$ mJy. The lower ALMA disc flux could be produced by spatial filtering in the ALMA data due to a lack of short baselines, as the maximum recoverable scale is 6 arcsec given the range of baselines in the data. This is illustrated in Fig. 3 and demonstrated in Section 4, where we fit and simulate the observed visibilities and the SCUBA2 image using a parametric disc model that we use to constrain the disc flux and disc surface density.

We search for any spatially resolved disc emission by azimuthally averaging a CLEAN image of the ALMA data spatially smoothing the emission tapering the visibilities with the Fourier transform of a Gaussian of FWHM of 1.5 arcsec. This process degrades the CLEAN beam to a size of 1.8 arcsec × 1.5 arcsec increasing the signal-to-noise ratio (S/N) for extended emission. The azimuthal averaging method also takes into account the disc inclination and PA and is done in wedges of ±30° along the major axis of the disc. At each radius, the uncertainty is computed based on the uncertainty on each pixel and the number of independent measurements, estimated to be equal to the length of the arc over which we are averaging, divided by the beam's semimajor axis. The azimuthally averaged intensity is presented in the bottom panel of Fig. 4. This shows a marginal disc detection of $0.04 \pm 0.01$ mJy beam$^{-1}$ at 5.5 arcsec ± 0.9 arcsec (where the positional uncertainty is roughly estimated as ∼beam semimajor axis/$\sqrt{\text{S/N}}$), equivalent to $47 \pm 8$ au, consistent with the inner disc radius constrained to be between 30 and 40 au, depending

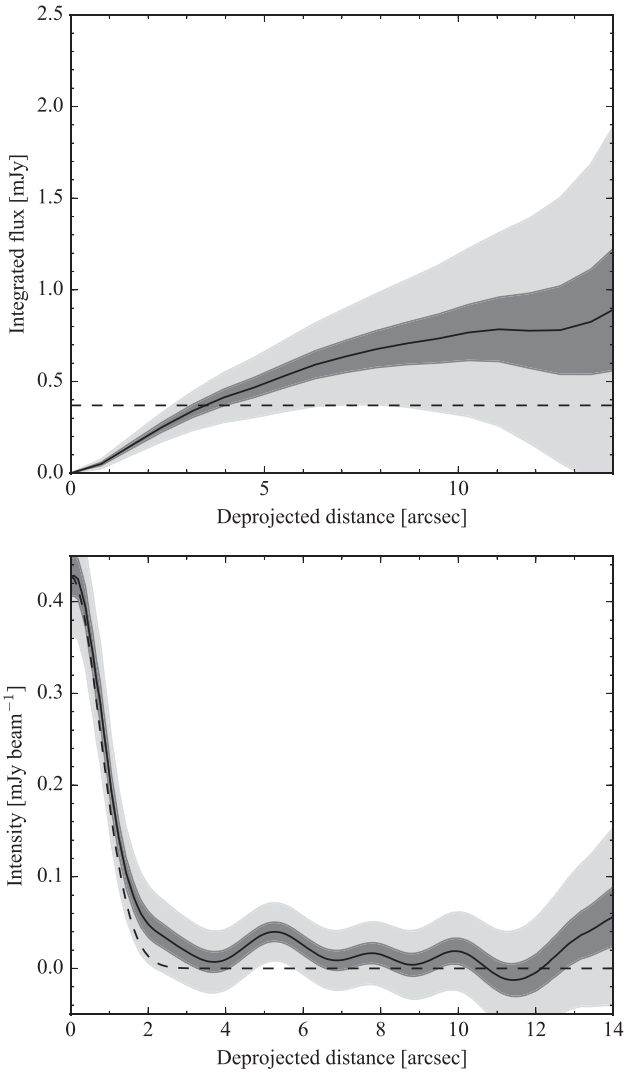


**Figure 4.** Top: integrated flux versus semimajor axis of elliptic regions over which the flux is integrated. The dashed line represents the stellar flux. Bottom: average intensity radial profile computed in wedges of ±30° along the major axis of the disc, using the reconstructed CLEAN image tapered with the Fourier transform of a Gaussian of FWHM of 1.5 arcsec. The dashed line represents the PSF. The grey shaded areas in both panels represent 68 and 99.7 per cent confidence regions.

on the disc model assumed to fit the *Herschel* observations (Wyatt et al. 2012). Moreover, positive emission, but not significantly above zero apart from the peak at 5.5 arcsec, is present from the stellar position to a distance of 11 arcsec. This is consistent with the positive total flux described before, in other words, with the $2.2\sigma$ detection integrated over all radii.

### 3.2 CO

Although CO gas of secondary origin has been found in a few young bright debris discs, probably released in collisions of icy solids (e.g. 49 Ceti, $\beta$ Pic, HD 131835, HD 181327 and Fomalhaut, Zuckerman, Forveille & Kastner 1995; Dent et al. 2014; Moór et al. 2015b; Marino et al. 2017; Matrà et al. 2017), no CO ($v = 0$, J = 3–2) emission was detected in 61 Vir ALMA data. Integrating the continuum-subtracted channel maps from 30 to 100 au and RV

in the range ±5.1 km s$^{-1}$ with respect to the stellar RV (expected Doppler shift due to Keplerian rotation at 30 au), we derive an integrated noise level of 27 mJy km s$^{-1}$. We can use this to place a 3$\sigma$ upper limit to any CO present in the disc. As shown by Matrà et al. (2015), non-local thermodynamic equilibrium effects can be significant in the low-density environments of debris discs; therefore, it is necessary to consider the effect of different gas kinetic temperatures and collisional partner densities – assumed to be electrons released from carbon ionization after the CO gas is photodissociated (as predicted by thermodynamic models; e.g. Kral et al. 2016). Using the tools developed by Matrà et al. (2015), we derive a CO gas mass upper limit of $1.4 \times 10^{-6}$ M$_\oplus$ using the 3$\sigma$ upper limit on the CO flux, the assumed disc extent (30–100 au) and a carbon ionization fraction of 0.5 and a C/CO abundance of 100 (assumed to be equal to those in $\beta$ Pic; Roberge et al. 2000; Cataldi et al. 2014), which fixes the ratio between electron and CO gas number densities in the disc.

Given the short photodissociation time-scale of 120 yr, together with the low dust optical depth, and thus, low collisional rates of solids in the disc, we do not expect to detect CO gas being released in collisions of icy planetesimals in this system. For example, if we assume that planetesimals in the disc have a CO mass fraction of 16 per cent, near the maximum fraction that has been observed in Solar system comets (0.3–16 per cent; Mumma & Charnley 2011) and similar to other systems with detected exocometary gas (Matrà et al. 2017), we expect only $\lesssim 10^{-9}$ M$_\oplus$ of CO gas in the disc coming out from collisions. Greater amounts of CO gas trapped in ices could come out from icy planetesimals closer in if these are scattered into highly eccentric orbits that can cross the $H_2O$ or $CO_2$ snow lines within 10 au, as suggested by recent ALMA observations of $\eta$ Corvi (Marino et al. 2017), but this is not detected and no evidence of such scattering has been found so far for 61 Vir.

## 4 DISC MODELLING

In order to place better constraints on the total disc flux, disc size, inclination and PA, we fit a parametric disc model to the SCUBA2 image and ALMA visibility data simultaneously. The model consists of a central star surrounded by a dusty disc and two background point sources (B1 and B2) at the position of the maxima in the ALMA image. The fluxes of the star, B1 and B2, are held fixed at their observed values of 0.37, 0.36 and 0.85 mJy, respectively. Note that the B2 is apparently resolved and could be modelled with an extended component, but this has no effect on the fitted parameters and best-fitting models.

The dusty disc is assumed to be composed of grains formed by astrosilicates (Draine 2003), amorphous carbon (Li & Greenberg 1998) and water ice (Li & Greenberg 1998), with mass fractions of 70 per cent, 15 per cent and 15 per cent, respectively. We mix the optical constants using the Bruggeman rule (Bohren & Huffman 1983) and mass-weighted opacities are computed using the Mie theory code of Bohren & Huffman (1983), assuming a Dohnanyi-like size distribution with a power-law index of −3.5 (Dohnanyi 1969), and minimum grain size of 1 μm, roughly the blow-out size, and a maximum size of 1 cm. We expect larger grains to be present, but we can neglect their thermal emission at this wavelength. The central star is modelled using a stellar template spectrum with an effective temperature of 5500 K[1] (Kurucz 1979) and a radius of 1.1 R$_\odot$ to fit the stellar emission at 0.86 mm. Then, the dust equilibrium temperature at different radii is computed using RADMC-3D[2] (Dullemond et al. 2016). The disc surface density varies with radius and is parametrized with a power-law function as $r^\alpha$ from a minimum radius of 30 au, extending to $R_{\rm max}$, which is a free parameter as well as $\alpha$ and the total disc flux, $F_{\rm disc}$. We maintain $R_{\rm min}$ fixed at 30 au (best-fitting value for a model with a sharp inner edge when fitting the *Herschel* observations and SED; Wyatt et al. 2012). The vertical mass distribution is assumed to be Gaussian with a standard deviation or scaleheight $H$ that scales linearly with radius as $H = 0.1r$. Synthetic images at 0.86 mm are then produced using RADMC-3D with an inclination, $i$, and PA that are also left as free parameters. In total, there are five free parameters that we vary to fit the observations.

Model visibilities are computed at the same UV points as the ALMA observations (e.g. Marino et al. 2015, 2017, 2017). To speed up the simulation of model visibilities, we average the ALMA data with a time and frequency bin of 90 s and 1.88 GHz, respectively. This averaging is small enough both in time and frequency to ensure that the time and frequency smearing are smaller than 0.1 arcsec (≪ synthesized beam). We simulate the SCUBA2 observation by convolving the model image with a two-dimensional Gaussian with an FWHM of 13 arcsec.

To find the best fit we use a Bayesian approach, sampling the parameter space using the PYTHON module EMCEE, which implements Goodman & Weare's Affine Invariant MCMC Ensemble sampler (Goodman & Weare 2010; Foreman-Mackey et al. 2013). The posterior distribution is defined as the product between the likelihood function and our prior distributions. The first is defined as $\exp(-\chi^2/2)$, with $\chi^2 = \chi^2_{\rm ALMA} + \chi^2_{\rm SCUBA2}$, with

$$\chi^2_{\rm ALMA} = \sum_i \frac{||V_{{\rm data},i} - V_{{\rm model},i}||^2}{\delta V^2_{{\rm data},i}}, \quad (1)$$

where the sum goes over the UV points of the previously averaged visibilities, $V_{{\rm data},i}$. The estimated error $\delta V_{{\rm data},i}$ is calculated based on the intrinsic dispersion of the visibilities over one scan with the task STATWT from CASA 4.7. On the other hand, $\chi^2_{\rm SCUBA2}$ is defined as the squared sum over every pixel of the difference between the SCUBA2 and model image (convolved with the 13 arcsec beam), divided by the pixel rms. The pixel rms is empirically estimated by measuring the dispersion on the unsmoothed SCUBA image that has uncorrelated pixel noise.

The prior probabilities of the parameters are assumed to be uniform. We restrict $R_{\rm max}$ to be between 30 and 250 au, $\alpha$ from −5 to 5, $F_{\rm disc} > 0$, PA from 0° to 90° and $i$ from 45° to 90° (priors based on the previous *Herschel* observations).

To demonstrate that there is disc emission in the ALMA data that can be better constrained by adding the SCUBA2 image to the fitting process, in Fig. 5 we present the marginalized distributions of $i$ and PA when fitting only the ALMA data and constraining $R_{\rm max}$ to values below 140 au as any disc emission beyond that would lie outside the ALMA primary beam. Even though disc emission above 3$\sigma$ is not present in the reconstructed ALMA image (see Fig. 2), but only when integrating the emission, we find that the disc orientation can still be constrained and matches with the previous estimates from *Herschel* observations (blue lines).

Table 1 and Fig. 6 present the best fit parameters and marginalized distributions of $R_{\rm max}$, $\alpha$ and $F_{\rm disc}$, when ALMA visibilities and

[1] http://www.stsci.edu/hst/observatory/crds/k93models.html

[2] http://www.ita.uni-heidelberg.de/~dullemond/software/radmc-3d/

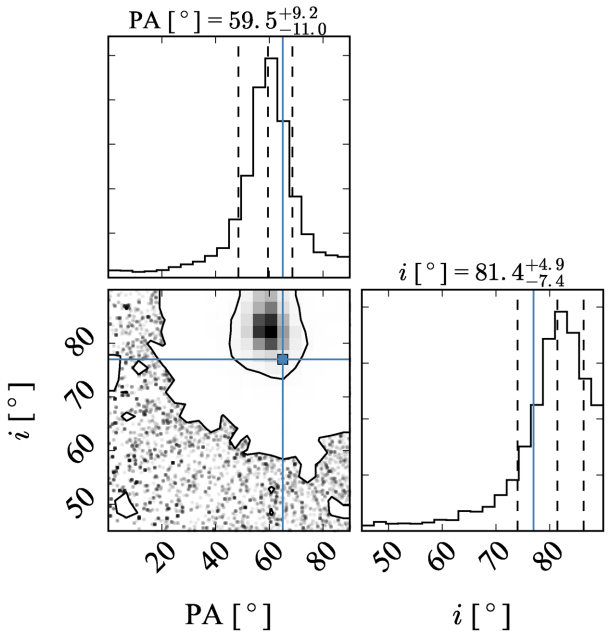


**Figure 5.** Posterior distributions of PA and $i$ when fitting the ALMA data only. The vertical dashed lines represent the 16th, 50th and 84th percentiles. Contours correspond to 68 per cent and 95 per cent confidence regions. The blue lines represent the previous estimates of $i$ and PA from *Herschel* observations. This plot was generated using the PYTHON module CORNER (Foreman-Mackey et al. 2014).

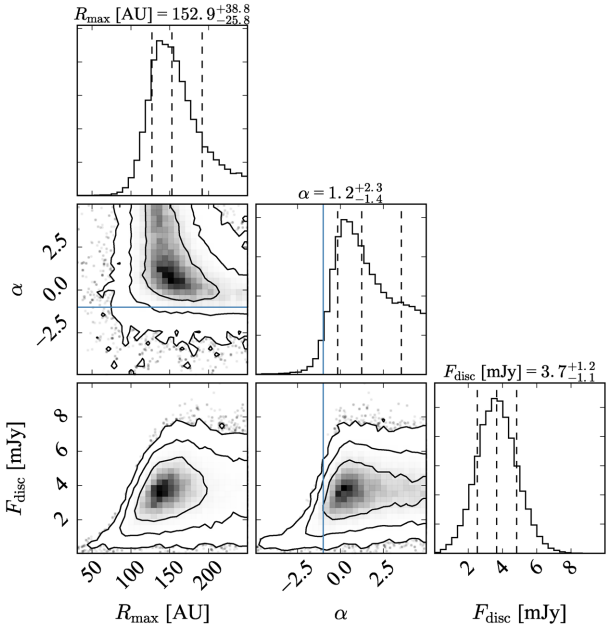


**Figure 6.** Posterior distribution of $R_{max}$, $\alpha$ and $F_{disc}$. The vertical dashed lines represent the 16th, 50th and 84th percentiles. Contours correspond to 68 per cent, 95 per cent and 99.7 per cent confidence regions. The blue lines represent the previous estimate of $\alpha$ from *Herschel* observations. This plot was generated using the PYTHON module CORNER (Foreman-Mackey et al. 2014).

**Table 1.** Best-fitting values of the ALMA and SCUBA2 data combined. Median ± uncertainty based on the 16th and 84th percentile of the marginalized distributions.

| Parameter | Best-fitting value |
|---|---|
| $R_{max}$ (au) | $153^{+39}_{-26}$ |
| $\alpha$ | $1.2^{+2.3}_{-1.4}$ |
| $F_{disc}$ (mJy) | $3.7^{+1.2}_{-1.1}$ |
| PA (°) | $59 \pm 5$ |
| $i$ (°) | $82 \pm 4$ |

the SCUBA2 image are combined in the analysis. The disc orientation is better constrained, with PA = 59 ± 5 and $i = 82° \pm 4°$, consistent with the *Herschel* observations (PA = 65° and $i = 77°$), and within the limits obtained from fitting the ALMA data alone (see Fig. 5). Regarding the disc structure, we find that $\alpha$ peaks at zero on its marginalized posterior distribution and is constrained between −0.2 and 3.5 (68 per cent confidence), but still consistent within the 95 per cent confidence region with the value of −1 (see Fig. 6) found by fitting the *Herschel* observations, which was also poorly constrained (Wyatt et al. 2012). If we restrict $i$ between 70° and 80° (using the prior information from *Herschel* images), we can improve our constraints on the slope, finding $\alpha = 0.1^{+1.1}_{-0.8}$. Therefore, we conclude that the surface density distribution is not very centrally concentrated.

For example, we can discard a scattered disc that has an initial characteristic surface density proportional to $r^{-3.5}$ (e.g. Duncan & Levison 1997). The collisional evolution of such a scattered disc has been studied analytically by Wyatt et al. (2010). We find that for 61 Vir parameters, i.e. assuming $t = 4.6$ Gyr, $\alpha = 2.5$, pericentre at 30 au and $M_{disc} \sim 10^{-2}$–$10^{2}$ $M_{\oplus}$, the resulting surface density should be significantly peaked at 30 au (pericentre) and decrease steeply with radii, inconsistent with our observations (see their fig. 5). Although the analytic model used by Wyatt et al. (2010) could overestimate the surface density of dust at low radii as it is the case for low eccentricities.

On the other hand, a flat distribution could be expected in the context of an extended disc with a wide range of semimajor axes and small eccentricities, collisionally evolved after being stirred (e.g. Schüppler et al. 2016; Geiler & Krivov 2017, see Section 5). We also find that $R_{max}$ is peaked at ∼150 au, consistent with the maximum radius of at least 100 au derived with *Herschel*. However, if $\alpha < 0.5$ then the maximum radius is not well constrained as the surface brightness decreases with radius [$B(r) \propto r^{\alpha - 0.5}$]. $F_{disc}$ peaks above zero (3.4$\sigma$), and is constrained to be $3.7^{+1.2}_{-1.1}$ mJy; however, this is highly dependent on $R_{max}$ and $\alpha$. For example, if $\alpha \sim -1$ then $F_{disc} < 4$ mJy (95 per cent confidence).

We also try to vary $R_{min}$ and leave it as a free parameter, but we find that it is not well constrained in these observations. The posterior marginalized distribution of $R_{min}$ is close to flat with a peak at the inner boundary set to 5 au. With a smaller $R_{min}$, the disc surface brightness decreases which fits best the ALMA visibilities, while conserving the total flux to fit the SCUBA observations. Therefore, we decide to leave $R_{min}$ fixed based on the previous *Herschel* and SED information that are inconsistent with $R_{min} \ll 30$ au.

In Fig. 7, we compare simulated observations of different models and their residuals when subtracted from the real observations. The first column shows the best-fitting model from the posterior distribution presented above with a total flux of 3.5 mJy, $\alpha = 0$, $R_{max} = 150$ au, PA=65° and $i = 77°$, which has a reduced chi-squared $\chi^2_{red} = 1.002\ 8838$ ($N \sim 6 \times 10^6$). The second column shows a model with $\alpha = -1.0$, $R_{max} = 250$ au and $F_{disc} = 2$ mJy, i.e. the most likely disc flux for this $\alpha$. This model is still consistent with having no disc emission above 3$\sigma$ in the reconstructed image

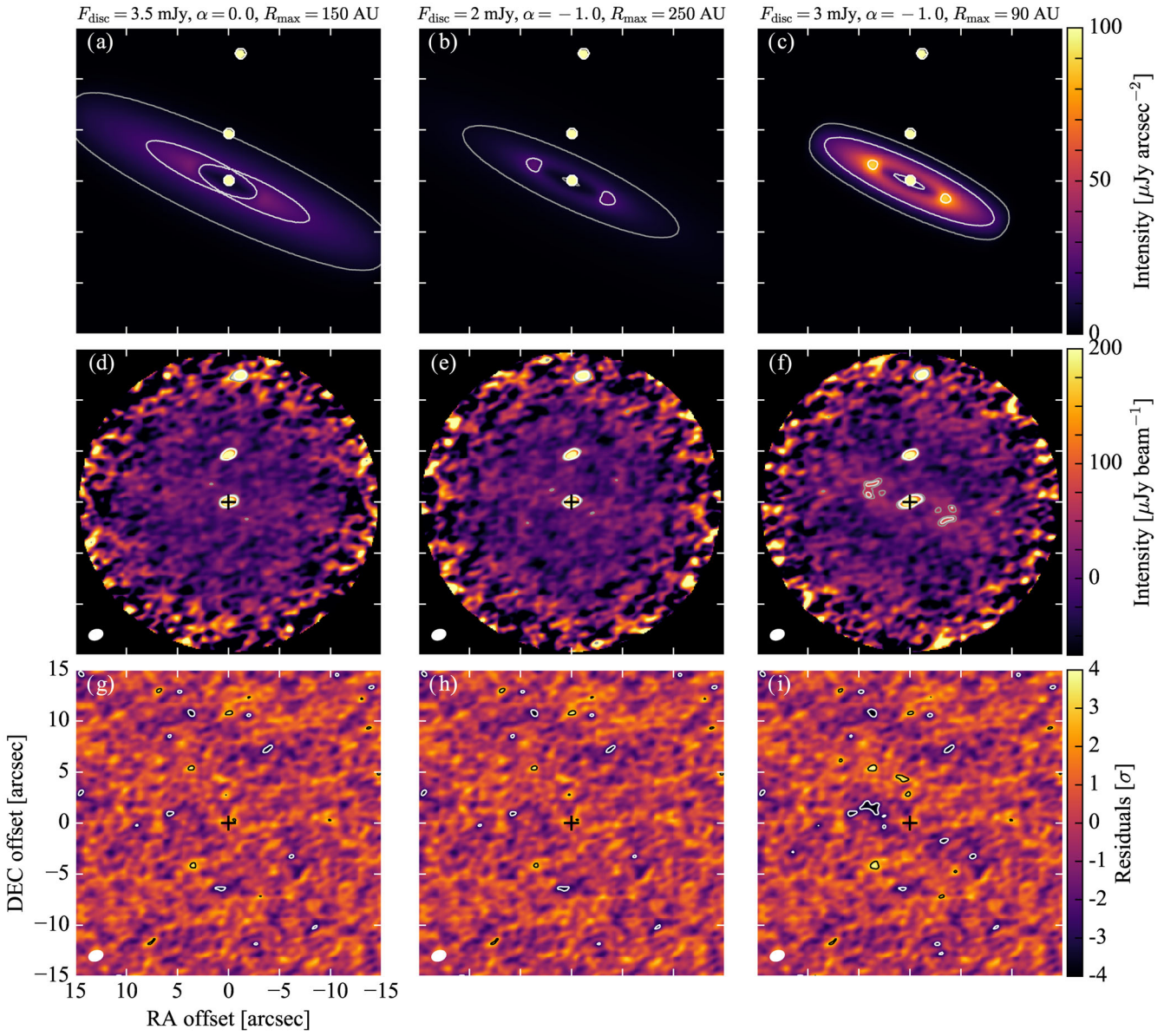


**Figure 7.** Simulated model images and residuals at 0.86 mm. First column: $F_{\rm disc} = 3$ mJy, $\alpha = 0$, PA $= 65^\circ$ and $i = 77^\circ$. Second column: $F_{\rm disc} = 3.5$ mJy, $\alpha = -1$, PA $= 65^\circ$ and $i = 77^\circ$. Third column: $F_{\rm disc} = 6$ mJy, $\alpha = -1$, PA $= 65^\circ$ and $i = 77^\circ$. First row: synthetic images of the disc. Contours represent 5, 20 and 80 μJy arcsec$^{-2}$. Second row: primary beam corrected simulated ALMA CLEAN images using the same uv-sampling and adding Gaussian noise to the visibilities, according to their variance in the observations. Contours represent three, four and five times the local noise level. Third row: dirty map of the ALMA residuals after subtracting the model visibilities from the ALMA observations. The noise level on the residuals is uniform and equal to 16 μJy beam$^{-1}$ as they are not corrected by the primary beam. The black and white contours represent $\pm 3\sigma$. The beam size is represented by a white ellipse in the bottom left corner. The *x*- and *y*-axes indicate the offset from the stellar position in RA and Dec. in arcsec, i.e. north is up and east is left. The stellar position is marked with a black '+'.

and has $\chi^2_{\rm red} = 1.002\,8840$ ($1.4\sigma$ difference with the first model). The third column corresponds to a model similar to the second, but with a less extended disc with $R_{\rm max} = 90$ au and $F_{\rm disc} = 3$ mJy, increasing the surface brightness of the disc to levels above $3\sigma$ in the simulated observation (Fig. 7f), which translates to significant negative residuals (Fig. 7i) and $\chi^2_{\rm red} = 1.002\,8897$ ($35\sigma$ difference with the previous model). We also find that the image reconstruction suffers from flux loss due to an insufficient number of short baselines and the size of the primary beam (17 arcsec). For the models in the first, second and third columns, we recover integrated fluxes of 0.6, 1.0 and $2.3 \pm 0.2$ mJy, respectively. From the best-fitting values of the parameters (i.e. $R_{\rm max} \gtrsim 150$ au), the SCUBA2 measured flux ($5.0 \pm 1.2$ mJy) and the simulated observations which show that a compact disc would be detectable, we conclude that the disc of planetesimals must be broad and not concentrated in a single or a few narrow rings, which could not have been resolved by *Herschel* (model 3 in Section 1).

## 5 STEADY-STATE COLLISIONALLY EVOLVED DISC MODEL

It is generally assumed in debris discs that the surface density of millimetre-sized grains can be simply scaled to derive the distribution of the total solid mass in discs. This is true under the assumption

that the size distribution from big to small bodies remains fixed. However, using detailed numerical simulations with the Analysis of Collisional Evolution (ACE) code (Krivov, Löhne & Sremčević 2006), Schüppler et al. (2016) recently showed that the radial profile of the vertical optical depth can deviate considerably from the distribution of planetesimals, when considering this more realistic model of how the grain size distribution evolves at different radii. For example, when assuming a maximum planetesimal size of 100 and 200 km in diameter, they found that the optical depth (dominated by the smallest grains in the disc) stays roughly constant as a function of radius between 10 and 100 au, even though the total surface density decreases with radius. This effect is not due to radiation pressure affecting small dust grains, but due to the evolution of the size distribution at different radii. Specifically, the difference arises when the largest planetesimals in the disc (that dominate the disc mass) are not collisionally evolved, but the smallest grains are already in collisional equilibrium. Using a three phase analytic model for the size distribution, Geiler & Krivov (2017) confirmed this effect and explored how it changes depending on the primordial conditions of the disc.

This implies that even if we assume that the primordial distribution of solids in a debris disc is close to a standard Minimum Mass Solar Nebula (MMSN) with a radial distribution with an exponent of $-1.5$ after the protoplanetary disc disperses (Weidenschilling 1977a; Hayashi 1981), or any model for the initial surface density profile of an accreting protoplanetary disc (e.g. Kuchner 2004; Raymond, Quinn & Lunine 2005; Chiang & Laughlin 2013), the radial distribution of dust grains with lifetimes shorter than the age of the system could have a significantly different radial dependence. Therefore, the surface density exponent for millimetre grains derived in Section 4 cannot be simply extrapolated to the total surface density of solids in 61 Vir.

Here, we aim to study the expected surface density of millimetre grains in a broad debris disc undergoing collisional evolution, and how that depends on the choice of maximum planetesimal size. We do this by using a simple numerical prescription that simulates the size distribution using size bins and assuming that the size distribution is in quasi-steady-state. This means that the mass-loss rate due to catastrophic collisions in each size bin is balanced by the input from fragmentation of larger bodies in destructive collisions, which inputs mass into the bin. The maximum size in collisional equilibrium, $D_c$, corresponds to the one having a collisional lifetime equal to the age of the system. This method is described in detail in Wyatt, Clarke & Booth (2011, see sections 2.4.2, 2.5 and 2.9 therein) and can reproduce the morphology (slope and wiggles) seen in more detailed numerical simulations (e.g. using the ACE code; Löhne, Krivov & Rodmann 2008).

Our model is composed of a 1 $M_\odot$ star at the centre and a debris disc spanning 1–300 au. The primordial mass surface density of solids is assumed to be that of an MMSN: $\Sigma_0(r) = (r/1\,\mathrm{au})^{-1.5}\,M_\oplus\,\mathrm{au}^{-2}$, with an initial size distribution of solids proportional to $D^{-3.7}$, though the main results presented below are independent of this choice. The minimum size of solids in the cascade is set to 0.8 μm, which is the blow-out size assuming a star of 1 $L_\odot$ and 1 $M_\odot$, and an internal density of solids of 2700 kg m$^{-3}$. Grains smaller than this are immediately lost from the disc. We explore different maximum diameters ($D_{\max}$) between 1 and 100 km. The disc is assumed to be pre-stirred or stirred on a time-scale much shorter than the age of the system, i.e. initially having velocities high enough so collisions between planetesimals are destructive and result in a collisional cascade. This is accounted by setting the mean eccentricity ($e$) and inclination ($I$) of the particles to be 0.05 and 1°.4 ($e/2$), respectively, which defines the relative velocities of the particles. These velocities are calculated as $v_{\rm rel} = v_{\rm K}(1.25e^2 + I^2)^{1/2}$ (valid for Rayleigh distributions of $e$ and $I$; Lissauer 1993; Wetherill & Stewart 1993), where $v_{\rm K}$ is the Keplerian velocity on a circular orbit. Hence, the relative or impact velocities are a 6 per cent of $v_{\rm K}$.

Furthermore, in our model destructive collisions are only caused by impactors with specific energies greater than the disruption threshold or planetesimal strength ($Q^\star_{\rm D}$), which depends both on the size and impact velocity. The disruption threshold has been studied in laboratory experiments (e.g. Fujiwara et al. 1989; Davis & Ryan 1990; Ryan, Hartmann & Davis 1991) and with numerical simulations of colliding basalt and icy bodies (e.g. Benz & Asphaug 1999). It is well known that for small bodies bound by cohesive binding forces, $Q^\star_{\rm D}$ decreases with size up to the size where self-gravity becomes important, and then $Q^\star_{\rm D}$ increases with size. Therefore, we assume the following prescription:

$$Q^\star_{\rm D} = \left[ Q_{\rm D,s} \left( \frac{\rm D}{1\,\rm m} \right)^{b_{\rm s}} + Q_{\rm D,g} \left( \frac{\rm D}{1\,\rm m} \right)^{b_{\rm g}} \right] \left( \frac{v_{\rm rel}}{v_0} \right)^{1/2}, \quad (2)$$

where $Q_{\rm D,s}$, $Q_{\rm D,g}$, $b_{\rm s}$ and $b_{\rm g}$ are parameters that depend on the specific composition of solids in the disc. The dependence on the relative or impact velocity is inspired by the results from Stewart & Leinhardt (2009). We use $Q_{\rm D,s} = 500$ J kg$^{-1}$, $Q_{\rm D,g} = 0.03$ J kg$^{-1}$, $b_{\rm s} = -0.37$, $b_{\rm g} = 1.36$ and $v_0 = 3$ km s$^{-1}$ values consistent with Basalt in simulations from Benz & Asphaug (1999). The choice of Basalt is not important for the results presented below. Using the values estimated for planetesimals composed of ice from the same study, we obtain similar results. Finally, we assume a 'redistribution function' for the fragments created in a destructive collision proportional to $D^{-3.5}$, with the largest fragment having half the mass of the original disrupted body. The specific dependence on $D$ does not change our results presented below.

We divide the disc in different independent annuli, each one with a total mass of $2\pi r \Delta r \Sigma_0(r)$, with $\Delta r = 2er$, which fixes the initial total mass in each radial bin. At a given radius, we solve for the steady-state size distribution by equating the mass-loss rate and gain in each size bin that is smaller than $D_{\rm c}$, the largest object that is in collisional equilibrium. The mass in size bins larger than $D_{\rm c}$ is held fixed to the primordial distribution as they have lifetimes or collisional time-scales longer than the age of the system and have not had enough time to significantly evolve. The time-scale to reach quasi-steady-state or damp perturbations is the same as the collisional time-scale; therefore, our quasi-steady-state assumption is valid for sizes smaller than $D_c$. To find the specific $D_c$, we solve for the steady-state size distribution varying $D_c$, until finding the specific size bin with a lifetime equal to the age of the system (or with a difference smaller than a 10 per cent). In the resulting size distribution bins for planetesimals larger than $D_c$ retain their original masses, while the masses in all smaller bins are anchored to $D_c$ and their size distribution is set by the collisional equilibrium condition. As the system age increases, $D_c$ increases, and the size distribution evolves, and thus, the total and mm-sized dust mass too.

If $D_c > D_{\max}$, i.e. the lifetime of the biggest planetesimal is shorter than the age of the system ($t_{\rm age}$), the mass in every bin is scaled as

$$M(r, t, D) = M'_0(D) \frac{t_{\rm c}(0)}{t_{\rm age}}, \quad (3)$$

where $t_{\rm age}$ is the age of the system, and $M'_0$ is the mass distribution in collisional equilibrium when $D_c = D_{\max}$, or when the system

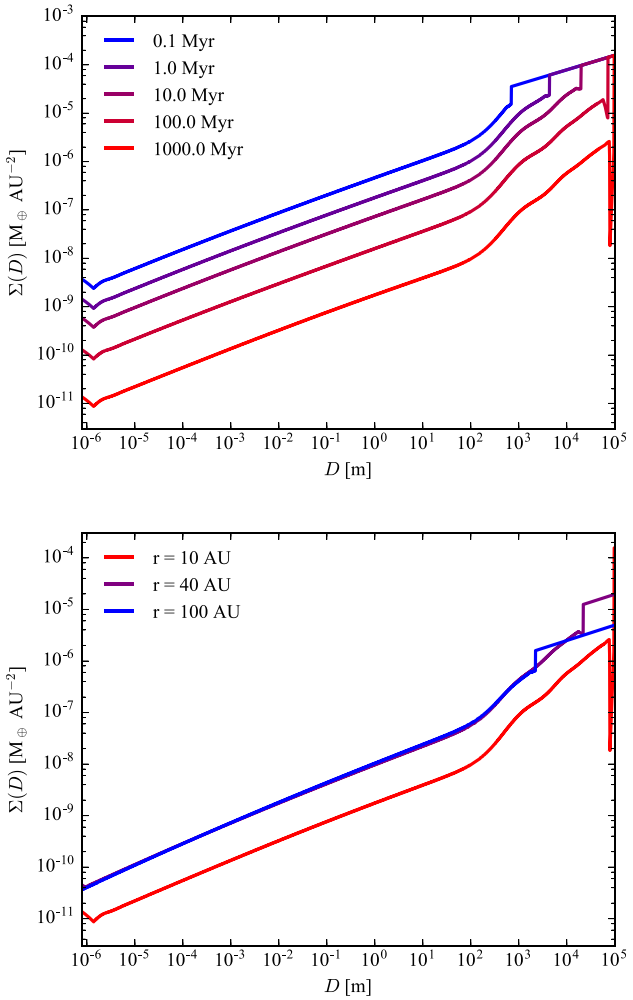


**Figure 8.** Mass surface density in each of the 3000 size bins spaced logarithmically, with $D_{\rm max} = 100$ km and $\Sigma_0 =$ MMSN. Top: size distribution at 10 au for a system age ranging from 0.1 Myr to 1 Gyr. Bottom: size distribution at 10, 40 and 100 au (red, purple and blue lines, respectively) for a system age of 1 Gyr.

had an age equal to the lifetime of the biggest planetesimal, $t_{\rm c}(0)$. Equation (3) is valid if the mass-loss rate is proportional to $M^2$, which is the case in our models as the collisional lifetime is inversely proportional to the mass in the cascade. The evolution of the surface density of solids at 10 au is illustrated in the top panel of Fig. 8. The main relevant feature of this evolution is that when $D_c < D_{\rm max}$, the mass in the small-sized bins decreases more slowly than it would when the entire size distribution is in equilibrium ($D_c = D_{\rm max}$).

In Fig. 9, we present the evolution of three discs varying $D_{\rm max}$ from 1 to 100 km (top and middle), and changing the stellar mass and luminosity together with $\Sigma_0$ and $D_{\rm max}$ to fit 61 Vir disc properties (bottom panel), i.e. its surface density of mass in mm-sized grains and disc inner edge (see Section 5.1). The surface density of the total mass in solids ($\Sigma$, left-hand column) evolves with time similarly to analytic models (e.g. Wyatt et al. 2007), increasing with distance as expected up to the characteristic radius, $r_{\rm c}$, at which the largest planetesimal in the disc has a lifetime equal to the age of the system, i.e. $t_{\rm c}(0) = t_{\rm age}$, and from there decreasing with radius as $\Sigma_0(r)$. This radius depends on the initial total solid mass and on $D_{\rm max}$ as the three panels in the first column show, with $r_{\rm c}$ being smaller for larger $D_{\rm max}$ or lower initial mass as the rate of collisions is reduced. The surface density of mass in mm-sized grains ($\Sigma_{\rm mm}$, right-hand column) behaves in a way similar to the optical depth described in Schüppler et al. (2016) and fractional luminosity in Geiler & Krivov (2017), mimicking $\Sigma(r)$ for $r < r_{\rm c}$, but considerably flatter compared to $\Sigma(r)$ at $r > r_{\rm c}$. This is because $D_c < D_{\rm max}$ and $D_c$ decreases with $r$ outside $r_{\rm c}$, so $\Sigma_{\rm mm}$ is less depleted for larger $r$. The net effect is that $\Sigma_{\rm mm}(r)$ is almost constant, even though $\Sigma(r)$ decreases with $r$.

To illustrate the differences in the evolved size distribution at different radii, in the bottom panel of Fig. 8 we compare the size distribution at 1 Gyr with $D_{\rm max} = 100$ km and $r = 10$, 40 and 100 au. At 10 au (red line), the disc evolves fast as relative velocities are higher and all the size bins are in collisional equilibrium. At 40 au (purple line), relative velocities are slower, hence $D_c \sim 20$ km and only smaller bodies are in collisional equilibrium; therefore, the mass in small bodies is highly depleted compared to the primordial, while the total mass in solids has not decreased significantly. At 100 au (blue line), relative velocities are even slower, $D_c \sim 2$ km and the mass in small bodies is less depleted compared to the primordial than at 40 au. Even though the surface density of the total mass in solids at $t = 0$ and 1 Gyr is higher at 40 au than at 100 au, the mass surface density in solids smaller than 1 km is approximately the same at both radii after 1 Gyr. This causes the slope of $\Sigma_{\rm mm}$ to flatten out and be almost constant at large radii where $t_{\rm c}(0) > t_{\rm age}$ as mentioned above. We also observe a very similar evolution for the vertical optical depth in the disc, consistent with Schüppler et al. (2016).

This behaviour that makes $\Sigma_{\rm mm}$ to be almost flat can be understood analytically if we consider a planetesimal strength approximated by two broken power laws and a continuous size distribution with three regimes: (i) small bodies in collisional equilibrium with a size distribution proportional to $D^{-q_1}$; (ii) large bodies with gravity-dominated strengths in collisional equilibrium with a size distribution proportional to $D^{-q_2}$ and (iii) largest planetesimals with lifetimes longer than the age of the system that conserve their primordial size distribution proportional to $D^{-q_3}$. The value of $q_1$ and $q_2$ are strictly related to the dependence on $D$ for $Q^\star_{\rm D}$, with (Durda & Dermott 1997; O'Brien & Greenberg 2003)

$$q_i = \frac{21 + b_i}{6 + b_i}, \tag{4}$$

where $b_i$ is the slope or exponent of $Q^\star_d$ in the strength or gravity-dominated regime. Therefore, assuming reasonable values for $b_{\rm s}$, $b_{\rm g}$ and $q_3$, we can find an analytic expression for the size distribution at different radii (e.g. Löhne et al. 2008). Moreover, assuming an initial surface density or mass distribution in the disc, we can derive an expression for the fractional luminosity as a function of radius, as shown by Shannon & Wu (2011, equation A10 therein) and Geiler & Krivov (2017, equation A11 therein). As the fractional luminosity is proportional to the surface density of small grains, we can rewrite equation A10 in Shannon & Wu (2011) to find

$$\Sigma_{\rm mm}(r) \propto \left[r^2 \Sigma_0(r)\right]^{\frac{2+k_2-k_2 q_2}{2+q_2-q_3+k_2-k_2 q_2}} r^{-2+\frac{(19+2q_2)(q_2-q_3)}{6(2+q_2-q_3+k_2-k_2 q_2)}}, \tag{5}$$

where $\Sigma_0(r)$ is the primordial total surface density of solids, and $k_2$ is equal to $\frac{6-q_2}{q_2-1}$ and represents the size scaling of the minimum impactor size to cause a catastrophic collision. The expression above is only valid when $D_c$ is less than $D_{\rm max}$, but large enough so it is in the gravity-dominated regime ($D_c \gtrsim 100$ m). Assuming $q_1$=3.6,

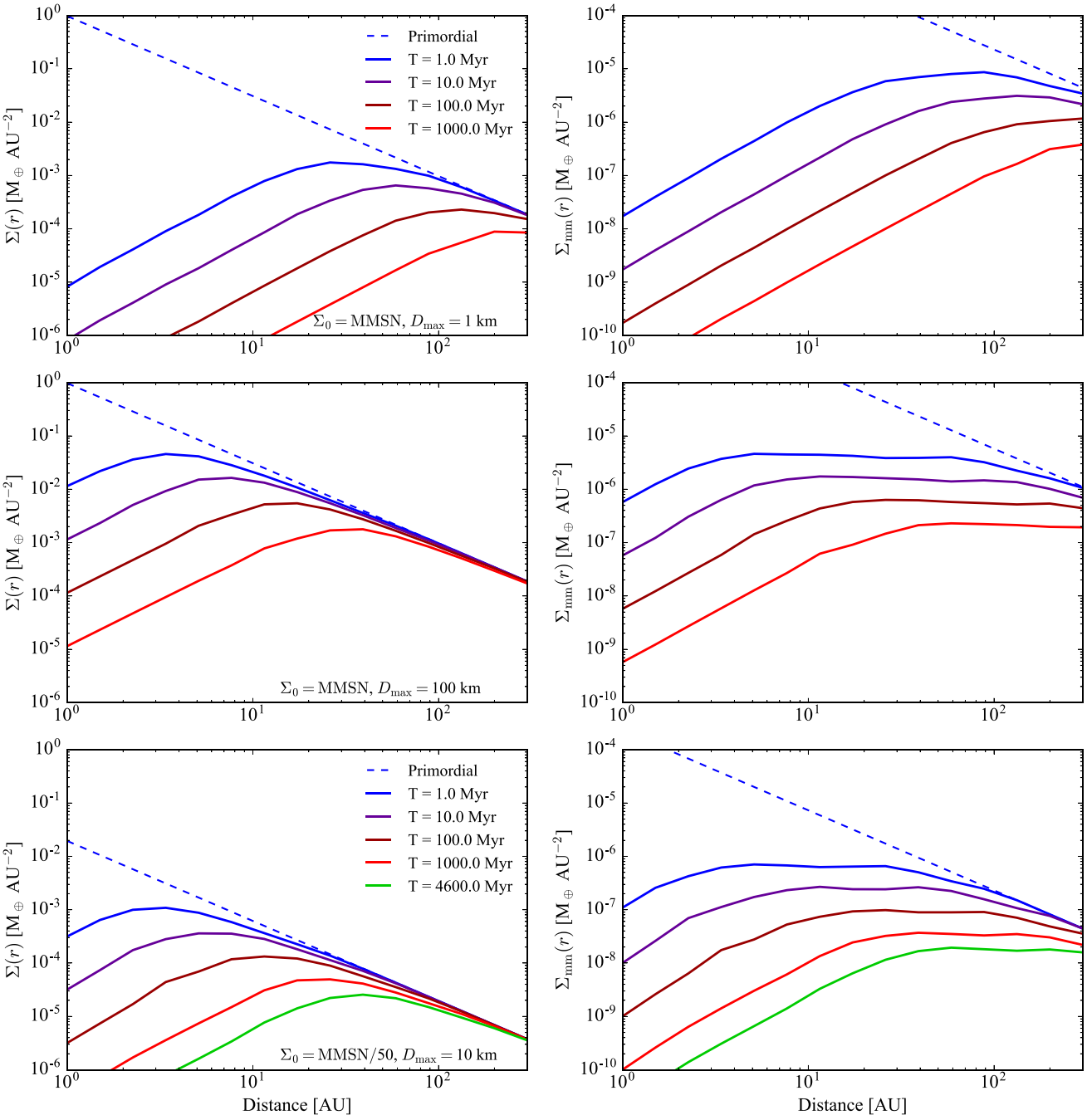


**Figure 9.** Total (left-hand column) and millimetre-sized dust mass (right-hand column) evolution of a disc from 1 to 300 au. The different rows represent the evolution of a disc with the following parameters: (top) solar type star with a primordial surface density equal to an MMSN and a maximum planetesimal size of 1 km; (middle) solar type star with a primordial surface density equal to an MMSN and a maximum planetesimal size of 100 km; (bottom) central star of 0.88 $M_\odot$ and 0.84 $L_\odot$ with a primordial surface density equal to 0.02 MMSN and a maximum planetesimal size of 5 km. The colours represent five different ages: 1, 10, 100, 1000 and 4600 Myr, varying from blue to red and green as time evolves.

$q_2$=3.0, $k_2 = 1.5$ (values consistent with $b_{\mathrm{s}}$ and $b_{\mathrm{g}}$ used above), $q_3 = 3.7$ and $\Sigma_0(r) = \Sigma_0(r/1\,\mathrm{au})^{\alpha}$, we find

$$\Sigma_{\mathrm{mm}}(r) \propto r^{0.6\alpha+0.9}. \quad (6)$$

Therefore, for $\alpha = -1.5$, $\Sigma_{\mathrm{mm}}$ is independent of radius, which matches with our more detailed numerical simulation. Moreover, the flatter $\Sigma_{\mathrm{mm}}$ in the evolved size distribution compared to the primordial distribution is independent of $\alpha$ as equation (6) shows; although a steeper primordial surface density of solids decreasing with radius would result in a steeper surface density of millimetre-sized grains with a slope of $0.6\alpha + 0.9$. For $q_3 = 3.5$ and 3.9, we still find a flat slope for $\Sigma_{\mathrm{mm}}$ of $-0.3$ and 0.2, respectively. From the results in our simulations, we can estimate the dependence of $\Sigma_{\mathrm{mm}}$ on $t$, $D_{\mathrm{max}}$ and $\Sigma_0$, by assuming a power-law dependence and fitting it to our numerical results. Coupling these with the dependence on $r$ from equation (6) (only valid for $q_1 = 3.6$, $q_2 = 3.0$ and $q_3 = 3.7$),

we find

$$\Sigma_{\rm mm}(r > r_{\rm c}) \approx 2 \left(\frac{r}{1\ {\rm au}}\right)^{0.6\alpha+0.9} \left(\frac{t}{1\ {\rm Gyr}}\right)^{-0.4} \left(\frac{D_{\rm max}}{100\ {\rm km}}\right)^{-0.1} \times \left(\frac{\Sigma_0}{1\ {\rm MMSN}}\right)^{0.6} {\rm M}_\oplus {\rm au}^{-2}, \quad (7)$$

where $\Sigma_0$ is the initial surface density of solids at 1 au in units of the MMSN. The factor 2 and the exponents of $-0.4$, $-0.1$ and 0.6 are the results from a fit to the numerical simulations. Equation (7) is only valid for $r > r_{\rm c}$ and $D_c \gtrsim 100$ m. Using equation A5 in Shannon & Wu (2011), we can also estimate how $r_{\rm c}$ varies with time and $\Sigma_0$. Moreover, from our simulations we can derive a dependence on $D_{\rm max}$ fitting a power law. We find

$$r_{\rm c} \approx 4 \left(\frac{t}{1\ {\rm Myr}}\right)^{1/(-\alpha+1.5)} \left(\frac{\Sigma_0}{1\ {\rm MMSN}}\right)^{1/(-\alpha+1.5)} \times \left(\frac{D_{\rm max}}{100\ {\rm km}}\right)^{-0.5} {\rm au}. \quad (8)$$

Assuming a specific dependence of planetesimal strength on size, equations A10 from Shannon & Wu (2011), and equations (7) and (8) from this work, together with the disc model presented above, can be used to retrieve the primordial radial distribution of solids from ALMA observations of extended discs if the biggest planetesimals in the disc still conserve their primordial size distribution. Moreover, they can be used to constrain the initial total mass in the disc and maximum planetesimal size. So far, there is no evidence of extended debris discs at millimetre wavelengths with a steep slope decreasing with radius (or non-consistent with being flat; e.g. Booth et al. 2016); however, even with ALMA (the most sensitive instrument at millimetre wavelengths), the detection and study of extended debris discs is only possible around a few of the brightest systems.

It is worth noting that the maximum planetesimal size in a disc could vary with radius by orders of magnitude as the growth timescales for planetesimals are a steep function of radius and the surface density in solids (e.g. Kenyon & Bromley 2008). Moreover, stirring could have stopped the growth at different epochs for different radii. Although in our models we assume that the maximum planetesimal size is independent of radius, our prediction for $\Sigma_{\rm mm}(r > r_{\rm c})$ in equation (7) is not very sensitive to $D_{\rm max}$. Therefore, our predictions are reasonably valid even if the maximum planetesimal size decreases with radius (as expected in planet formation models). This is already illustrated in Fig. 9. If we consider a disc with $D_{\rm max}$ decreasing from 100 to 1 km between 40 and 300 au, then the resulting $\Sigma_{\rm mm}(r)$ at 1 Gyr would be almost the same as the red line in the middle right panel on that figure, because $\Sigma_{\rm mm}(300\ {\rm au})$ increases only by a factor of 2 when decreasing $D_{\rm max}$ from 100 to 1 km. This is due to two opposite effects: (1) for a constant total mass in solids, reducing $D_{\rm max}$ increases the mass in millimetre-sized dust; and (2) reducing $D_{\rm max}$ makes the collisional evolution faster that reduces the mass in every bin in collisional equilibrium. A similar effect would be present at $r < r_{\rm c}$ making the surface density slope flatter. The maximum planetesimal size is only significantly important to determine $r_{\rm c}$. The opposite scenario, and less likely, in which $D_{\rm max}$ increases with radius would result in a slightly steeper slope for both $r < r_{\rm c}$ and $r > r_{\rm c}$.

Other differences relative to our assumptions could also change the slope of the millimetre surface density, such as the epoch of stirring (in our simulations we consider a pre-stirred disc), or the mean eccentricity and inclination of particles in the disc, or even the disruption threshold of planetesimals and dust if their composition varies with radius. For example, a different $Q_{\rm D}^\star$ would modify the size distribution, changing the slope of the predicted millimetre surface density as equation (5) shows.

### 5.1 Application to 61 Vir

In Section 4, we find that the observations in the millimetre are best fitted with a disc extending to ∼150 au, an integrated flux of $3.7 \pm 1.2$ mJy and a flat surface density distribution, equivalent to a dust mass of $\sim 2 \times 10^{-8}$ M$_\oplus$ au$^{-2}$. In addition, the minimum radius derived from a best-fitting model of a collisionally evolved disc to the *Herschel* observations is ∼40 au. Using the same model for the collisional evolution of a disc described above (replacing the stellar mass and luminosity with 0.88 M$_\odot$ and 0.84 L$_\odot$; Sousa et al. 2008; Wyatt et al. 2012), we find a best match with a primordial surface density between 20 and 100 times less dense than the MMSN and a maximum planetesimal size between 5 and 20 km. These two parameters determine that $t_{\rm c}(0) = 4.6$ Gyr at ∼40 au and $\Sigma_{\rm mm}(r) \sim 2 \times 10^{-8}$ M$_\oplus$ au$^{-2}$ for $r > 40$ au.

The need for a low primordial surface density and a maximum planetesimal size of 10 km is due to the low mass in millimetre grains, which scales roughly as $D_{\rm max}^{-0.1} \Sigma_0^{0.6}$ (see equation 7), together with a large $r_{\rm c}$, that scales roughly as $D_{\rm max}^{-0.5} \Sigma_0^{0.33}$ (see equation 8). Therefore, we need a very low $\Sigma_0$ to fit the millimetre surface density and a low $D_{\rm max}$ to have $r_{\rm c} \sim 40$ au given the low $\Sigma_0$. From the size distribution, we can also determine a vertical optical depth of $2 \times 10^{-4}$, a few times higher than the optical depth from *Herschel* observations and SED fitting, but still consistent considering all the assumptions made in both modelling efforts. For example, a more detailed treatment of radiation pressure could change the value of the optical depth by a factor of a few. The derived maximum planetesimal size and primordial surface density go in the same direction as the ones from Wyatt et al. (2012); the primordial surface density of solids in the disc was much lower compared to the MMSN and with a maximum planetesimal size not much larger than 10 km.

## 6 DISCUSSION

### 6.1 A depleted broad disc of planetesimals

In Section 4, we found that the debris disc in 61 Vir is broad, extending from 30 to 150 au or larger radii. If the emission was concentrated in a few $\lesssim$20 au wide rings of planetesimals, the disc would have been detected above $3\sigma$ in the ALMA map. Moreover, the $2.2\sigma$ difference between the flux measured by SCUBA2 and ALMA is indicative that there is flux loss in the reconstructed ALMA image due to the disc emission being mostly in structures on scales larger than 6 arcsec (50 au); and thus not recoverable by the range of baselines in the ALMA data. This was corroborated using simulated observations of different broad disc models. Therefore, we conclude that the planetesimal disc must be extended with a wide range of semimajor axes. A different scenario with a population of highly eccentric planetesimals with a small range of semimajor axes is discarded as the derived surface density is flatter than expected in a scattered disc scenario (e.g. Duncan & Levison 1997) and while collisional erosion can flatten this distribution by preferentially eroding the inner regions, this cannot completely erase the density enhancement at the inner edge of the disc (Wyatt et al. 2010).

The inner edge of the disc could be defined by the collisional evolution that has been ongoing for 4.6 Gyr as assumed in Section 5,

or instead the disc could have been truncated by a yet unseen planet. In the first scenario, the observed inner edge of the disc (30–40 au) can be explained by a maximum planetesimal size of only about 10 km and primordial surface density of solids 50 times lower than an MMSN. One explanation for why the planetesimals did not grow to larger sizes could be the low surface density of solids that slows down the growth time-scales (Kenyon & Bromley 2008), but could also be because the planetesimals were stirred by a planet closer in hindering their growth.

In the second scenario, in which the inner edge of the disc has been truncated by a planet, the maximum planetesimal size is no longer constrained to be of the order of ∼10 km. However, even if we consider a maximum planetesimal size of 1000 km, the mass of the primordial disc still needs to be a factor of ∼10 lower compared to an MMSN in order to fit the flat surface density of millimetre grains derived in this paper and the *Herschel* observations (Wyatt et al. 2012). This depletion could arise from the protoplanetary disc phase if the disc had a low mass, or a low efficiency of planetesimal formation, or due to radial drift of solid particles during that gas-rich phase that concentrated most of the solid mass in the inner regions (Whipple 1973; Weidenschilling 1977b). The radial drift of solids could have also contributed to an *in situ* formation of the two to three planets found within 1 au of the star (e.g. Hansen & Murray 2012).

A variant on the second scenario involves the 30 au truncation radius being caused by a planet that is no longer present. For example, if the close-in planets formed further out (just inside 30 au) and then migrated to their current location accreting and scattering planetesimals on their way in, the early evolution of these close-in planets could be responsible for both the truncation of the outer disc and its stirring (e.g. Alibert et al. 2006; Terquem & Papaloizou 2007; Kennedy & Kenyon 2008; Payne et al. 2009; Ida & Lin 2010).

### 6.2 Stirring by a yet unseen planet

If 61 Vir b and c formed *in situ*, then something else must have stirred the disc as these are too far in and not massive enough to have stirred the disc at large radii within 4.6 Gyr (Wyatt et al. 2012). Hence, we propose that an unseen planet at a larger distance and within the 30 au disc inner edge stirred the disc. Similar to Moór et al. (2015a), using equation 6 from Mustill & Wyatt (2009, valid for planets with eccentricities $\lesssim$0.3), we can derive lower limits on the eccentricity of such a planet depending on its semimajor axis and mass so the time-scale of stirring is shorter than the age of the system. Moreover, the eccentricity imposed on the planetesimals ($e_f$) must be higher than a certain value so that their relative velocities are high enough to cause destructive collisions ($v_{rel,max} \sim 2e_f v_K$). Here, we impose that the forced eccentricity (equation 8 in Mustill & Wyatt 2009) must be higher than 0.01, so planetesimals of 5 km diameter undergo destructive collisions with planetesimals of the same size at 150 au. This is illustrated in Fig. 10. The minimum eccentricity decreases with increasing semimajor axis and planet mass as the time-scale for stirring is held fixed at 4.6 Gyr. The forced eccentricity must be >0.01, which results in a kink in the 0.1 contour (because $e_f$ is independent of mass). All other contours are set by the stirring time set equal to the age of the system.

We can add additional constraints if we require planets with a pericentre that does not get closer than 5 mutual Hill radii (see equation 9 in Pearce & Wyatt 2014) from the apocentre of 61 Vir c ($a = 0.22$ au, $e = 0.14$), i.e.

$$a_{plt}(1 - e) - 5R_{H,q} > a_c(1 + e_c), \quad (9)$$

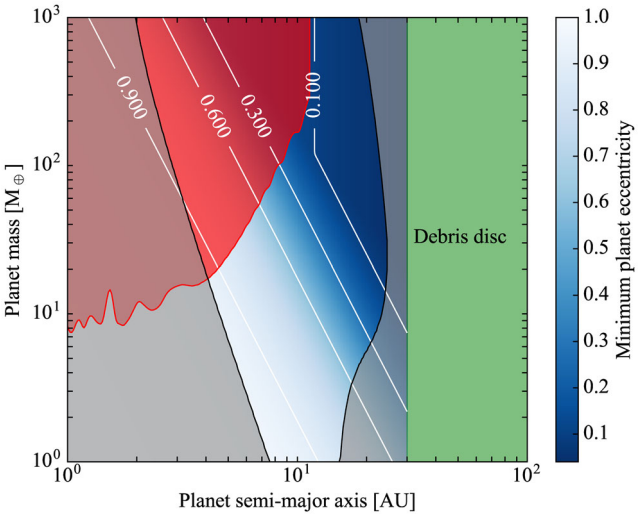


**Figure 10.** Allowed masses and semimajor axes for a putative planet that stirred the 61 Vir debris disc out to 150 au, in a time-scale shorter than 4.6 Gyr, and forcing an eccentricity higher than 0.01. The blue colour map and white contours represent the minimum eccentricity for a given planet mass and semimajor axis. The green shaded region on the right is excluded as the planet would overlay with the inner edge of the disc at 30 au. The grey shaded region is excluded as those planets would get closer than 5 Hill radii to 61 Vir c or to the inner edge of the disc. Finally, the red region in the top left corner is excluded from upper limits based on RV data.

where $R_{H,q}$ is the Hill radii at pericentre and $a_c$ and $e_c$ are the semi-major axis and eccentricity of 61 Vir c. In addition, the apocentre of the hypothetical planet d has to be such that it does not get closer than 5 Hill radii to the disc inner edge at ∼30 au. These two constraints exclude the grey shaded area. Because lower mass planets have higher eccentricity, the maximum semimajor axis decreases with decreasing planet mass for $M_{plt} \lesssim 10$ M$_\oplus$, but also decreases with increasing planet mass as the $R_{H,q}$ gets larger. Finally, using upper limits from RV data from HARPS, we can exclude planets more massive than the red line (Wyatt et al. 2012; Kennedy et al. 2015).

With these limits on $M_{plt}$ and $a_{plt}$, we can conclude that if an unseen planet interior to the debris disc is responsible for stirring the planetesimals up to 150 au, and has an eccentricity lower than 0.1, then it must be more massive than 10 M$_\oplus$ and have a semimajor axis between 10 and 20 au. Less massive planets and closer in ($a_{plt} = 4$–20 au) could have stirred the disc, but with $e \gg 0.1$. For the allowed combinations of $M_{plt}$ and $a_{plt}$, even a highly eccentric planet will not induce an eccentricity higher than the observed on 61 Vir b and c or cause close encounters (see fig. 5 in Read & Wyatt 2016). Moreover, an eccentric planet will impose an eccentricity on the disc that may be detectable by imaging of the disc (Wyatt et al. 1999). While there is no evidence of any asymmetry, the constraints are weak, both because the imaging is in the far-IR where the transition from pericentre to apocentre glow occurs (Pan, Nesvold & Kuchner 2016), and because the disc would look symmetric if the pericentre is aligned with the minor axis of the disc projected in the sky.

The equations used to derive the minimum eccentricity are only valid for $e_{plt} \lesssim 0.3$. Planet eccentricities higher than 0.3 could be overestimated as the predicted stirring time-scales are longer than expected for $e > 0.3$ (see fig. 1 in Mustill & Wyatt 2009). Therefore, the lower limits presented in Fig. 10 are only representative of the constraints expected for $e_{plt} \lesssim 0.3$.

### 6.3 Background sources

As noted before by Wyatt et al. (2012), none of the detected compact sources (B1 and B2) are comoving with 61 Vir, therefore, we can assume these are background objects. B1 together with B3 and its northern counterpart (that lies outside the ALMA primary beam) are probably related to an active galactic nucleus (AGN; Condon et al. 1998). B1 at the centre is consistent with compact emission from dust heated by an AGN, or with flat-spectrum synchrotron emission typical of a radio galaxy core, or with dust associated with a nuclear starburst, or some combination of these possibilities. On the other hand, the two lobes are consistent with synchrotron emission that we do not expect to detect in the submillimetre (submm), given their steep spectra.

The most northern source detected by ALMA (B2) was previously detected by *Herschel* from 160 to 500 μm and is resolved by the ALMA synthetic beam with a size of ∼2 arcsec. This is larger than expected for the $z$∼1–3 submm galaxy population (e.g. Smail, Ivison & Blain 1997), where ALMA has measured typical submm sizes of ≪1 arcsec (e.g. Ikarashi et al. 2015; Simpson et al. 2015), slightly smaller than their typical radio sizes (Biggs et al. 2011), but is consistent with a dusty starburst at a rather lower redshift, as we would suspect from its relatively blue PACS/SPIRE SED.

## 7 SUMMARY AND CONCLUSIONS

We have presented the first resolved millimetre study of 61 Vir, a planetary system with two confirmed RV planets within 1 au and a debris disc at tens of astronomical units. Combining ALMA and SCUBA2/JCMT observations, we found that at 0.86 mm the total disc emission is 3.7 ± 1.2 mJy, the disc extends from 30 to at least 150 au, and has surface density exponent of millimetre grains of $0.1^{+1.1}_{-0.8}$. This implies that the parent planetesimal disc is broad with a wide range of semimajor axes. The alternative scenario of a highly scattered disc with planetesimals with a common pericentre is discarded given the constraints on the surface brightness of the disc. No CO gas emission was detected in the disc, although even if planetesimals are rich in CO and releasing gas through collisions, we predict that any emission should be below our detection limit.

We developed a full disc collisional evolution model based on previous numerical work that can reproduce some of the results obtained in more detailed simulations, but in a much more computationally efficient approach. These models predict that the surface density of millimetre grains and optical depth radial profiles do not necessary match with the surface density of the parent bodies, tending to be flatter in regions of the disc where the age of the system is shorter than the collisional lifetime of the biggest planetesimals. This can be used to constrain the primordial surface density distribution of solids and maximum planetesimal size for extended discs for reasonable assumptions on the eccentricity, inclination and strength of planetesimals. For example, with this model we can reproduce the observations if 61 Vir debris disc started with a surface density ∼50 times more depleted in solids compared to an MMSN, and with planetesimals that did not grow more than 5–20 km in size so the disc is collisionally depleted at $r < 40$ au. However, these conclusions are based on the assumption that the inner edge of the observed disc is set by the collisional evolution of the disc. If instead the inner edge is set by other mechanism, e.g. planet–disc interaction, then the maximum planetesimal size is no longer constrained, but the primordial surface density would still need to be depleted by a factor of ∼10 compared to the MMSN.

Finally, we discussed and constrained the mass, semimajor axis and eccentricity of a planet stirring the disc located between the known RV planets and the inner edge of the disc. We found that in order to have stirred the disc out to 150 au, the planet must be more massive than 10 $M_\oplus$ and a semimajor axis between 10 and 20 au if it has an eccentricity lower than 0.1. Otherwise, for higher eccentricities it could have a lower mass and a semimajor axis between 4 and 20 au.

## ACKNOWLEDGEMENTS

We thank Pablo Roman and Simon Casassus for providing us the tool *uvsim* to simulate model visibilities. We also thank Matthew J. Read for useful discussion. This paper makes use of the following ALMA data: ADS/JAO.ALMA#2013.1.00359.S. ALMA is a partnership of ESO (representing its member states), NSF (USA) and NINS (Japan), together with NRC (Canada) and NSC and ASIAA (Taiwan) and KASI (Republic of Korea), in cooperation with the Republic of Chile. The Joint ALMA Observatory is operated by ESO, AUI/NRAO and NAOJ. MCW, LM and AS acknowledge the support of the European Union through ERC grant number 279973. GMK is supported by the Royal Society as a Royal Society University Research Fellow. AS is partially supported by funding from the Center for Exoplanets and Habitable Worlds. The Center for Exoplanets and Habitable Worlds is supported by the Pennsylvania State University, the Eberly College of Science and the Pennsylvania Space Grant Consortium.

## REFERENCES

Alibert Y. et al., 2006, A&A, 455, L25
Benz W., Asphaug E., 1999, Icarus, 142, 5
Biggs A. D. et al., 2011, MNRAS, 413, 2314
Bohren C. F., Huffman D., 1983, Absorption and Scattering of Light by Small Particles. Wiley, New York
Booth M. et al., 2016, MNRAS, 460, L10
Bryden G. et al., 2006, ApJ, 636, 1098
Bryden G. et al., 2009, ApJ, 705, 1226
Carpenter J. M. et al., 2009, ApJS, 181, 197
Cataldi G. et al., 2014, A&A, 563, A66
Cavanagh B., Jenness T., Economou F., Currie M. J., 2008, Astron. Nachr., 329, 295
Chapin E. L., Berry D. S., Gibb A. G., Jenness T., Scott D., Tilanus R. P. J., Economou F., Holland W. S., 2013, MNRAS, 430, 2545
Chiang E., Laughlin G., 2013, MNRAS, 431, 3444
Condon J. J., Cotton W. D., Greisen E. W., Yin Q. F., Perley R. A., Taylor G. B., Broderick J. J., 1998, AJ, 115, 1693
Davis D. R., Ryan E. V., 1990, Icarus, 83, 156
Dent W. R. F. et al., 2014, Science, 343, 1490
Dohnanyi J. S., 1969, J. Geophys. Res., 74, 2531
Dominik C., Decin G., 2003, ApJ, 598, 626
Draine B. T., 2003, ApJ, 598, 1017
Dullemond C., Juhasz A., Pohl A., Sereshti F., Shetty R., Peters T., Commercon B., Flock M., 2016, RADMC3D v0.40. Available at: http://www.ita.uni-heidelberg.de/dullemond/software/radmc-3d/
Duncan M. J., Levison H. F., 1997, Science, 276, 1670
Durda D. D., Dermott S. F., 1997, Icarus, 130, 140
Eiroa C. et al., 2013, A&A, 555, A11
Fontenla J. M., Balasubramaniam K. S., Harder J., 2007, ApJ, 667, 1243
Foreman-Mackey D., Hogg D. W., Lang D., Goodman J., 2013, PASP, 125, 306
Foreman-Mackey D., Price-Whelan A., Ryan G., Emily Smith M., Barbary K., Hogg D. W., Brewer B. J., 2014, triangle.py v0.1.1. Available at: http://dx.doi.org/10.5281/zenodo.11020
Fressin F. et al., 2013, ApJ, 766, 81

Fujiwara A., Cerroni P., Davis D., Ryan E., di Martino M., 1989, in Binzel R. P., Gehrels T., Matthews M. S., eds, Asteroids II. University of Arizona Press, Tucson, AZ, p. 240
Geiler F., Krivov A., 2017, MNRAS, 468, 959
Goodman J., Weare J., 2010, Commun. Appl. Math. Comput. Sci., 5, 65
Greaves J. S., Holland W. S., Jayawardhana R., Wyatt M. C., Dent W. R. F., 2004, MNRAS, 348, 1097
Hansen B. M. S., Murray N., 2012, ApJ, 751, 158
Hayashi C., 1981, Prog. Theor. Phys. Suppl., 70, 35
Hillenbrand L. A. et al., 2008, ApJ, 677, 630
Holland W. S. et al., 2013, MNRAS, 430, 2513
Howard A. W. et al., 2010, Science, 330, 653
Ida S., Lin D. N. C., 2010, ApJ, 719, 810
Ikarashi S. et al., 2015, ApJ, 810, 133
Kalas P. et al., 2008, Science, 322, 1345
Kennedy G. M., Kenyon S. J., 2008, ApJ, 682, 1264
Kennedy G. M. et al., 2015, MNRAS, 449, 3121
Kenyon S. J., Bromley B. C., 2008, ApJS, 179, 451
Kral Q., Wyatt M., Carswell R. F., Pringle J. E., Matrà L., Juhász A., 2016, MNRAS, 461, 845
Krivov A. V., Löhne T., Sremčević M., 2006, A&A, 455, 509
Kuchner M. J., 2004, ApJ, 612, 1147
Kurucz R. L., 1979, ApJS, 40, 1
Lagrange A.-M. et al., 2009, A&A, 493, L21
Li A., Greenberg J. M., 1998, A&A, 331, 291
Lissauer J. J., 1993, ARA&A, 31, 129
Löhne T., Krivov A. V., Rodmann J., 2008, ApJ, 673, 1123
Loukitcheva M., Solanki S. K., Carlsson M., Stein R. F., 2004, A&A, 419, 747
McMullin J. P., Waters B., Schiebel D., Young W., Golap K., 2007, in Shaw R. A., Hill F., Bell D. J., eds, ASP Conf. Ser. Vol. 376, Astronomical Data Analysis Software and Systems XVI. Astron. Soc. Pac., San Francisco, p. 127
Marino S., Casassus S., Perez S., Lyra W., Roman P. E., Avenhaus H., Wright C. M., Maddison S. T., 2015, ApJ, 813, 76
Marino S. et al., 2017, MNRAS, 460, 2933
Marino S. et al., 2017, MNRAS, 465, 2595
Marois C., Macintosh B., Barman T., Zuckerman B., Song I., Patience J., Lafrenière D., Doyon R., 2008, Science, 322, 1348
Marois C., Zuckerman B., Konopacky Q. M., Macintosh B., Barman T., 2010, Nature, 468, 1080
Matrà L. et al., 2017, preprint (arXiv:1705.05868)
Matrà L., Panić O., Wyatt M. C., Dent W. R. F., 2015, MNRAS, 447, 3936
Matrà L. et al., 2017, MNRAS, 464, 1415
Matthews B. C., Krivov A. V., Wyatt M. C., Bryden G., Eiroa C., 2014a, in Beuther H., Klessen R. S., Dullemond C. P., Henning T., eds, Protostars and Planets VI. Univ. Arizona Press, Tucson, AZ, p. 521
Matthews B., Kennedy G., Sibthorpe B., Booth M., Wyatt M., Broekhoven-Fiene H., Macintosh B., Marois C., 2014b, ApJ, 780, 97
Matthews B. C. et al., 2015, ApJ, 811, 100
Mayor M. et al., 2011, preprint (arXiv:1109.2497)
Montesinos B. et al., 2016, A&A, 593, A51
Moór A. et al., 2015a, MNRAS, 447, 577
Moór A. et al., 2015b, ApJ, 814, 42
Moro-Martín A. et al., 2007, ApJ, 658, 1312
Moro-Martín A. et al., 2015, ApJ, 801, 143
Mumma M. J., Charnley S. B., 2011, ARA&A, 49, 471
Mustill A. J., Wyatt M. C., 2009, MNRAS, 399, 1403
O'Brien D. P., Greenberg R., 2003, Icarus, 164, 334
Pan M., Nesvold E. R., Kuchner M. J., 2016, ApJ, 832, 81
Panić O. et al., 2013, MNRAS, 435, 1037
Payne M. J., Ford E. B., Wyatt M. C., Booth M., 2009, MNRAS, 393, 1219
Pearce T. D., Wyatt M. C., 2014, MNRAS, 443, 2541
Raymond S. N., Quinn T., Lunine J. I., 2005, ApJ, 632, 670
Raymond S. N. et al., 2011, A&A, 530, A62
Read M. J., Wyatt M. C., 2016, MNRAS, 457, 465
Roberge A., Feldman P. D., Lagrange A. M., Vidal-Madjar A., Ferlet R., Jolly A., Lemaire J. L., Rostas F., 2000, ApJ, 538, 904
Ryan E. V., Hartmann W. K., Davis D. R., 1991, Icarus, 94, 283
Schüppler C., Krivov A. V., Löhne T., Booth M., Kirchschlager F., Wolf S., 2016, MNRAS, 461, 2146
Shannon A., Wu Y., 2011, ApJ, 739, 36
Simpson J. M. et al., 2015, ApJ, 799, 81
Smail I., Ivison R. J., Blain A. W., 1997, ApJ, 490, L5
Smith B. A., Terrile R. J., 1984, Science, 226, 1421
Sousa S. G. et al., 2008, A&A, 487, 373
Stewart S. T., Leinhardt Z. M., 2009, ApJ, 691, L133
Su K. Y. L. et al., 2006, ApJ, 653, 675
Terquem C., Papaloizou J. C. B., 2007, ApJ, 654, 1110
Thébault P., Augereau J.-C., 2007, A&A, 472, 169
Thureau N. D. et al., 2014, MNRAS, 445, 2558
van Leeuwen F., 2007, A&A, 474, 653
Vican L., 2012, AJ, 143, 135
Vogt S. S. et al., 2010, ApJ, 708, 1366
Weidenschilling S. J., 1977a, Ap&SS, 51, 153
Weidenschilling S. J., 1977b, MNRAS, 180, 57
Wetherill G. W., Stewart G. R., 1993, Icarus, 106, 190
Whipple F. L., 1973, in Hemenway C. L., Millman P. M., Cook A. F., eds, Proc. IAU Colloq. 13: Evolutionary and Physical Properties of Meteoroids. Astron. Soc. Pac., San Francisco, p. 355
Wright N. J., Drake J. J., Mamajek E. E., Henry G. W., 2011, ApJ, 743, 48
Wyatt M. C., 2006, ApJ, 639, 1153
Wyatt M. C., Dermott S. F., Telesco C. M., Fisher R. S., Grogan K., Holmes E. K., Piña R. K., 1999, ApJ, 527, 918
Wyatt M. C., Smith R., Su K. Y. L., Rieke G. H., Greaves J. S., Beichman C. A., Bryden G., 2007, ApJ, 663, 365
Wyatt M. C., Booth M., Payne M. J., Churcher L. J., 2010, MNRAS, 402, 657
Wyatt M. C., Clarke C. J., Booth M., 2011, Celest. Mech. Dyn. Astron., 111, 1
Wyatt M. C. et al., 2012, MNRAS, 424, 1206
Zuckerman B., Forveille T., Kastner J. H., 1995, Nature, 373, 494

This paper has been typeset from a TEX/LATEX file prepared by the author.